

NIR SPECTROSCOPY OF THE HAeBe STAR HD 100546. III. FURTHER EVIDENCE OF AN ORBITING COMPANION?

SEAN D. BRITTAİN¹, JOHN S. CARR², JOAN R. NAJITA^{3,4}, SASCHA P. QUANZ⁵, AND MICHAEL R. MEYER⁵

¹ Department of Physics & Astronomy, 118 Kinar Laboratory, Clemson University, Clemson, SC 29634, USA; sbritt@clemson.edu

² Naval Research Laboratory, Code 7211, Washington, DC 20375, USA

³ National Optical Astronomy Observatory, 950 North Cherry Avenue, Tucson, AZ 85719, USA

⁴ Institute for Theory and Computation, Harvard-Smithsonian Center for Astrophysics, 60 Garden Street, Cambridge, MA 02138, USA

⁵ ETH Zurich, Institute for Astronomy, Wolfgang-Pauli-Strasse 27, 8093 Zurich, Switzerland

Received 2014 March 11; accepted 2014 July 9; published 2014 August 6

ABSTRACT

We report high-resolution NIR spectroscopy of CO and OH emission from the Herbig Be star HD 100546. We discuss how our results bear striking resemblance to several theoretically predicted signposts of giant planet formation. The properties of the CO and OH emission lines are consistent with our earlier interpretation that these diagnostics provide indirect evidence for a companion that orbits the star close to the disk wall (at ~ 13 AU). The asymmetry of the OH spectral line profiles and their lack of time variability are consistent with emission from gas in an eccentric orbit at the disk wall that is approximately stationary in the inertial frame. The time variable spectroastrometric properties of the CO $v = 1-0$ emission line point to an orbiting source of CO emission with an emitting area similar to that expected for a circumplanetary disk (~ 0.1 AU²) assuming the CO emission is optically thick. We also consider a counterhypothesis to this interpretation, namely that the variable CO emission arises from a bright spot on the disk wall. We conclude with a brief suggestion of further work that can distinguish between these scenarios.

Key words: circumstellar matter – protoplanetary disks – stars: formation – stars: individual (HD 100546) – techniques: spectroscopic

Online-only material: color figures

1. INTRODUCTION

Planet formation is a complex and poorly understood process (Helled et al. 2013). Yet candidate forming planets have been inferred in several protoplanetary disk systems based on studies of their spectral energy distributions and through direct imaging in the continuum (e.g., Quanz et al. 2013; Kraus & Ireland 2012; Huélamo et al. 2011). A low-mass accreting object in a transition disk has also been imaged in H α (Close et al. 2014). The Herbig B9e star HD 100546 has attracted recent attention as a system that may have forming low-mass, possibly planetary, companions (e.g., Quanz et al. 2013; Mulders et al. 2013; Brittain et al. 2013; Liskowsky et al. 2012; Panić et al. 2014). Located at a distance of 97 ± 4 pc (van Leeuwen 2007) and with an age of $\sim 3-10$ Myr (Manoj et al. 2006; van den Ancker et al. 1997), HD 100546 has a spectral energy distribution (SED) with a minimal near infrared (NIR) excess coupled with a substantial mid/far infrared (M/FIR) excess, i.e., it is a transition disk object. Modeling the SED, Bouwman et al. (2003) concluded that HD 100546 has a small disk in the inner few astronomical units and a much more massive disk beyond ~ 10 AU (see also Liu et al. 2003; Grady et al. 2005; Acke & van den Ancker 2006; Benisty et al. 2010; Quanz et al. 2011; Panić et al. 2014). Millimeter observations indicate that the dust mass of the disk is $5 \times 10^{-4} M_{\odot}$ (Henning et al. 1998). The large optically thin region between the inner disk and the outer disk suggests that the disk structure has evolved, possibly as a result of planet formation.

Stellar accretion is also ongoing in the system. Balmer lines with redshifted absorption components at ~ 220 km s⁻¹, consistent with magnetospheric accretion, have been observed toward HD 100546 (Guimarães et al. 2006). Modeling the Balmer discontinuity of HD 100546, Pogodin et al. (2012)

concluded that the accretion rate is $6 \times 10^{-8} M_{\odot} \text{ yr}^{-1}$. Despite this high accretion rate, the optically thin region of the disk appears to be clear of molecular gas. High-resolution infrared spectroscopy of rovibrational H₂ (Carmona et al. 2011), OH (Liskowsky et al. 2012; Paper I), and thermal-fluorescent CO emission (Brittain et al. 2009; van der Plas et al. 2009) find no molecular gas within ~ 13 AU of the star. Similarly, Habart et al. (2006) find that this inner region is also devoid of polycyclic aromatic hydrocarbon emission. Some atomic gas remains in the inner region of the disk, based on [O I] 6300 Å spectroscopy (Acke & van den Ancker 2006), which is not surprising given the continued stellar accretion. Thus, SED modeling, interferometry, direct imagery, and spectroscopy of warm molecules are all consistent with HD 100546 being an accreting transitional disk system whose inner 13 AU has been mostly (though not entirely) emptied of material.

Careful analysis of the CO and OH high-resolution spectroscopic observations provides possible evidence of an orbiting object near the disk wall at 13 AU. The asymmetric line profiles that we observed in the OH spectrum of HD 100546 are consistent with emission from an annulus with an eccentricity of ~ 0.2 (Paper I). Such a level of eccentricity can be produced by tidal interactions with a high-mass planetary companion on a circular orbit (Kley & Dirksen 2006). Because dynamical models predict that the semi-major axis of the eccentric annulus will precess very slowly ($\sim 10^{\circ}$ /1000 orbits; Kley & Dirksen 2006), we noted that if the asymmetric OH emission from HD 100546 arises from an eccentric annulus induced by a planetary companion, the line profile should not vary over timescales of months to years (Paper I).

The presence of an orbiting companion has also been inferred from non-axisymmetric structure in the gaseous CO $v = 1-0$ emission from HD 100546 (Brittain et al. 2013; Paper II).

Table 1
Log of Observations

Setting	Spectral Grasp (cm ⁻¹)	Integration (minutes)	S/N	Seeing (arcsec)	Centroid rms (mas)	Airmass (s(z))
L1	3135–3207	24	400	0.55	...	1.72
L2	3365–3448	35	230	0.73	...	2.08
M1	1998–2053	64	175	0.52	0.86	1.53

In contrast to the CO hotband emission from HD 100546, which showed no variability from 2003 to 2010, the line profile and spectroastrometric signal in the $\nu = 1-0$ CO emission from HD 100546 showed significant variability over the same period. We showed that the CO hotband emission could be explained as emission arising from an eccentric inner rim and an (axisymmetric) circumstellar disk beyond 13 AU. The spectroastrometric measurement of these emission lines confirmed the sense of rotation of the disk inferred from the spectroastrometric analysis of the [O I] 6300 Å line (Acke & van den Ancker 2006). The CO $\nu = 1-0$ emission could be fit as emission from a similar non-time-variable component (an eccentric inner rim and an axisymmetric circumstellar disk beyond 13 AU) plus a compact source of excess emission that varies in position and velocity as it orbits the star. The lower limit on the emitting area ($\sim 0.1 \text{ AU}^2$) of the orbiting component is similar to, but smaller than, the size predicted for a circumplanetary disk around a $5 M_{\text{Jup}}$ planet at a distance of 13 AU from HD 100546 (Ayliffe & Bate 2009; Martin & Lubow 2011a).

Thus, previous work offers evidence for a companion forming near the disk wall of HD 100546 and suggests ready made observational tests of this interpretation. In Paper II we noted that if this interpretation is correct the excess CO $\nu = 1-0$ emission would become blueshifted after 2010 while the line profiles of the hot band CO transitions would remain unchanged. Furthermore, the spectroastrometric signal of the blue side of the $\nu = 1-0$ line would become offset toward the east. In this paper, we present results from subsequent high-resolution L - and M -band spectroscopy of HD 100546 in 2013 which confirm our interpretation of the previous observations of rovibrational OH and CO emission from the HD 100546 disk. Observations such as these can potentially help us to understand the impact of forming planets on the circumstellar disk. They may also bear on the existence and nature of circumplanetary disks and the nature of the planetary accretion process.

2. OBSERVATIONS AND DATA REDUCTION

NIR spectra of HD 100546 were acquired with CRIFES on the European Southern Observatory Very Large Telescope (VLT) on 2013 March 18. The data were acquired with the 4 pixel ($0''.4$) slit without the use of adaptive optics. This instrumental configuration provides a resolving power of $R \sim 50,000$.

The L -band observations were taken with the slit at a position angle (P.A.) of 90° east of north. The M -band observations were taken with the slit at a P.A. of 90° and 140° as well as at the corresponding anti-parallel positions. In this paper we restrict our analysis to direct comparison to the previous results during which the slit P.A. was 90° . In a subsequent paper we will present the analysis and modeling of the full data set.

The FWHM of the point-spread function (PSF) of the continuum ranged from $0''.5-0''.7$ and the airmass of the observa-

Table 2
Flux of OH Emission lines

Line	Wavenumber (cm ⁻¹)	EqW (10 ⁻³ cm ⁻¹)	F_{line} (10 ⁻¹⁵ erg s ⁻¹ cm ⁻²)
P4.5(1+)	3407.99	4.56 ± 0.46	5.04 ± 0.50
P4.5(1-)	3407.61	5.99 ± 0.60	6.62 ± 0.66
P8.5(2-)	3194.28	2.97 ± 0.30	3.27 ± 0.33
P8.5(2+)	3193.69	3.10 ± 0.31	3.41 ± 0.34
P9.5(2-)	3146.18	1.55 ± 0.15	1.70 ± 0.17
P9.5(2+)	3145.49	2.62 ± 0.26	2.88 ± 0.29
P10.5(1+)	3142.06	1.81 ± 0.54	1.98 ± 0.59
P10.5(1-)	3141.04	2.85 ± 0.57	3.13 ± 0.63

tions ranged from 1.3–1.6. A summary of observations is presented in Table 1. Observations in the L and M bands are dominated by a strong thermal background. Therefore, an ABBA nod pattern between two positions separated by $\sim 10''$ was used to cancel the thermal background to first order. The CO emission can be detected out to $\sim 0''.7$ in each direction (Brittain et al. 2009); thus, there is no contamination between the beams.

The data are reduced using a customized set of routines based on algorithms developed for the reduction of data acquired with PHOENIX and NIRSPEC (see Brittain et al. 2007). Each AB pair of observations is combined in the sequence ($A-B$) and then divided by the normalized flat field image. The nod positions were jittered in a $2''$ box, so the median of the aligned images could be used to identify cosmic rays and bad pixels. The median of the aligned images was then compared to each of the individual frames. Pixels differing by more than 6σ from the median were rejected in the average.

The centroid of the PSF was measured by fitting a Gaussian curve to each column. For the M -band spectra, the centroid measurements of the parallel and anti-parallel beams were averaged to find the spectroastrometric offset of the spectra relative to the continuum. The one-dimensional spectra are formed by summing the 15 rows ($1/3$) centered on the PSF. The spectra were then wavelength-calibrated by fitting an atmospheric transmittance model generated by the Spectral Synthesis Program (Kunde & Maguire 1974), which accessed the 2000HITRAN molecular database (Rothman et al. 2003). The one-dimensional spectrum of HD 100546 was divided by the spectrum of the hot star standard α Cru. The telluric standard was observed at a similar airmass and scaled to provide an exact match (Figures 1 and 2). The S/N of the spectra and the fidelity of our centroid measurements are summarized in Table 1.

3. RESULTS

3.1. OH Emission

We detect the P4.5 ($1\pm$), 8.5($2\pm$), 9.5($2\pm$), and 10.5($1\pm$) lines at 1%–4% of the continuum (Figure 1). The equivalent widths of these lines were converted to relative fluxes using a spectrophotometric measurement of HD 100546 taken with the *International Space Observatory*. While we found that HD 100546 is variable in the NIR (Paper II), we assume for this analysis that the shape of the spectral energy distribution in the L -band has not varied. The relative flux of each line is presented in Table 2. By performing a linear least square fit to the points in the excitation diagram, we find that the rotational temperature of the OH gas is $1060 \pm 40 \text{ K}$ —consistent with the upper limit of 1400 K inferred from the previous observation. The equivalent

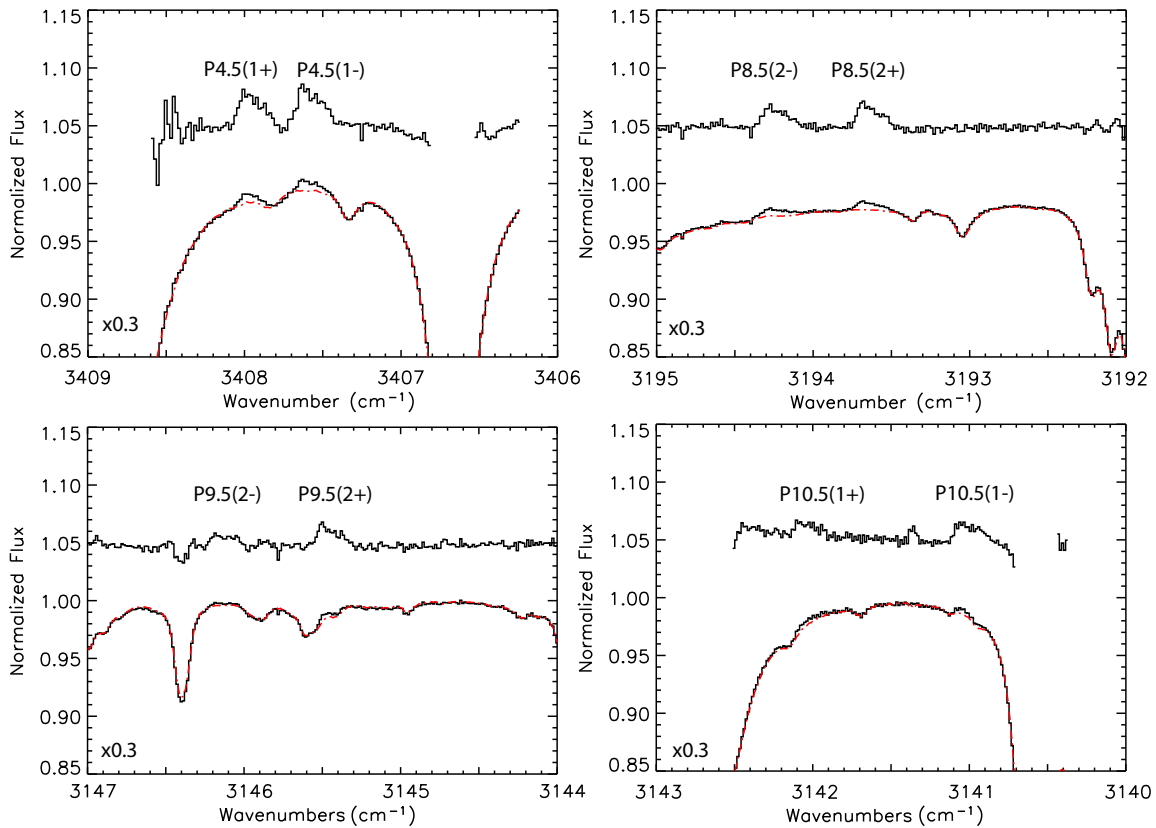


Figure 1. *L*-band spectra of HD 100546. The regions of the *L*-band spectra containing $\nu = 1-0$ OH emission lines are plotted. The telluric standard (red dot-dashed line) is plotted over the spectrum of HD 100546 (solid black line). The spectra are scaled by a factor of 0.3. The ratioed spectrum is plotted above the spectra and is offset +0.05 units. Regions where the atmospheric transmittance is less than 50% are omitted. The asymmetric line profile is apparent in the individual spectra.

(A color version of this figure is available in the online journal.)

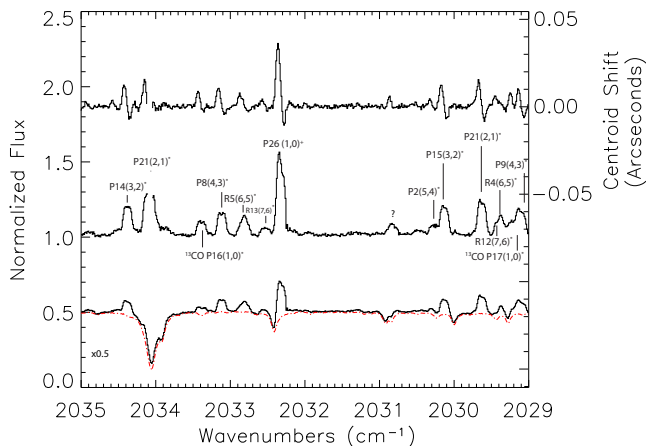


Figure 2. *M*-band spectrum of HD 100546. The portion of the *M*-band spectrum observed in previous epochs is plotted. The CO hotband and ^{13}CO lines are indicated by asterisks; these lines are excited by UV fluorescence. The most prominent emission line in the spectrum is the $\nu = 1-0$ P26 line near 2032.35 cm^{-1} (labeled with a “+”), which is excited by a combination of UV fluorescence and collisions. The spectrum of HD 100546 (solid black) and the telluric spectrum αCru (dot-dashed red) are scaled by a factor of 0.5 and plotted below the ratioed spectrum. Plotted above the ratioed spectrum is the spectroastrometric signal of the spectrum taken with the slit rotated to a position angle 90° E of N. The hotband lines are slightly asymmetric, and the $\nu = 1-0$ P26 line shows a much more dramatic asymmetry.

(A color version of this figure is available in the online journal.)

width of the OH emission lines decreased by 50% from 2010 December to 2013 March. This can be accounted for by a brightening of about 1 magnitude in the *L*-band—consistent with

the photometric variability of this object in the NIR (Paper II); however, we cannot rule out variation in the line fluxes.

We compare the profiles of the OH observed in 2013 with CRILES on the VLT and 2010 with PHOENIX on Gemini South (Figure 3(A)). In Paper I we showed that the asymmetric line shape could be fit if most of the emission arises from an eccentric annulus near disk wall. Over the span of 28 months, we see no evidence of variation of the line shape⁶ as predicted in Paper I if the eccentricity inferred from the line profile is induced by a companion.

3.2. CO Emission

We detect numerous fundamental rovibrational CO lines. For this paper we narrow our focus on the transitions overlapping our previous observations near the $\nu = 1-0$ P26 line (2029 cm^{-1} to 2035 cm^{-1} ; Figure 2). Comparison of the hot band lines observed in 2013 to the previous epochs shows only subtle variability in the shape of these lines (Figure 3(B)). However, like the OH lines, the equivalent widths of the hot band lines have varied. The 2013 equivalent widths are lower than those in 2010 by 30% and are consistent with the values measured in 2003. Despite these variations, the spectroastrometric signal of the hotband lines is similar in all four epochs and is consistent with emission from the circumstellar disk.

In contrast to the hot band lines, the line profile and spectroastrometric signal of the $\nu = 1-0$ P26 line have continued to

⁶ The use of the $0''.4$ slit is important in this respect. If we had observed the disk with the $0''.2$ slit with AO, then the observed line shape would depend sensitively on the pointing and the portion of the disk wall sampled (Hein Bertelsen et al. 2014).

Table 3
Properties of Excess CO $v = 1-0$ Emission

Date	Scaled Equivalent Width ^a (10^{-2} cm $^{-1}$)	Excess Equivalent Width (10^{-2} cm $^{-1}$)	Doppler Shift of Excess (km s $^{-1}$)	FWHM of Excess (km s $^{-1}$)	Position Angle of Excess	Orbital Phase of Excess ^b	Red Offset (mas)	Blue Offset (mas)
2003 Jan 7	4.50 ± 0.14	-40°	0°	12.7 ± 3.3	14.0 ± 3.3
2006 Jan 14	5.69 ± 0.59	1.19 ± 0.61	$+6 \pm 1$	6	-5°	$47^\circ \pm 10^\circ$	1.6 ± 4.3	17.8 ± 4.3
2010 Dec 23	6.39 ± 0.57	1.89 ± 0.58	-1 ± 1	12	60°	$97^\circ \pm 7^\circ$	5.7 ± 4.8	25.9 ± 4.8
2013 Mar 18	5.89 ± 0.20	1.12 ± 0.15	-6 ± 1	6	105°	$133^\circ \pm 10^\circ$	10.9 ± 0.9	35.8 ± 0.9

Notes.

^a The spectra were scaled such that the average hot band line profiles observed in 2006 and 2010 had the same equivalent widths as the average line profile observed in 2003.

^b The phase is measured counter clockwise from the northwest end of the semimajor axis of the disk.

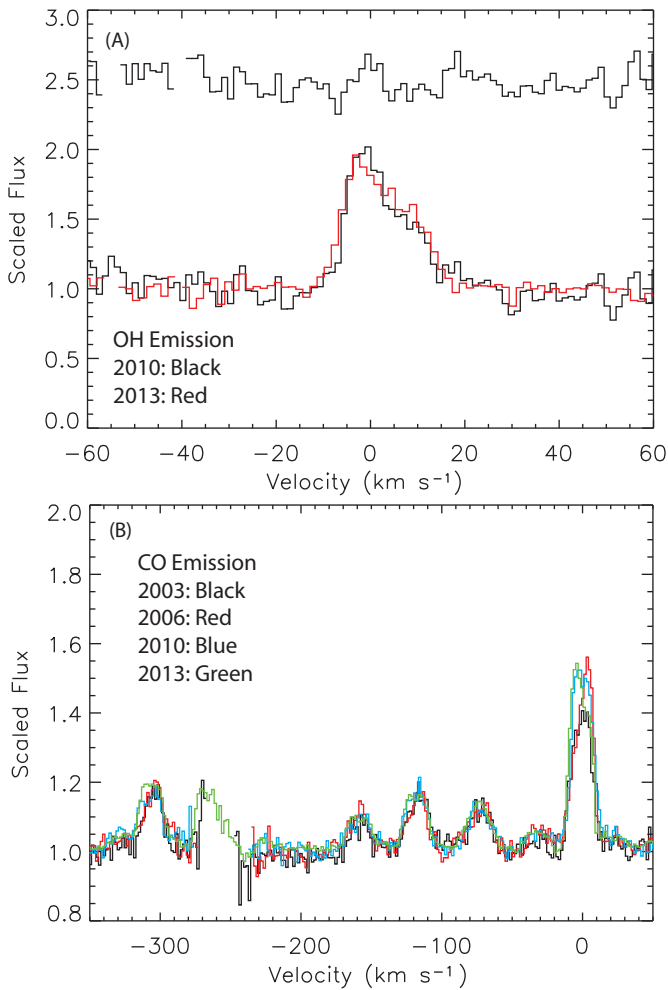


Figure 3. Multi-epoch observations of the OH (panel (A)) and CO (panel (B)) lines. In panel (A), the average of the OH emission lines observed in 2010 (black) and 2013 (red) are plotted over one another. Both lines have been scaled to a constant equivalent width. The difference between these spectra is plotted above. While the equivalent width of the lines varied, the shape of the lines has not varied within the signal to noise of our measurement. In panel (B) we plot the overlapping region of the CO spectra observed over four epochs. The spectra have been scaled so that the equivalent width of the average of the hotband lines is constant. While the shape of the hotband lines has not changed over the four epochs spanning 2003–2013, the $v = 1-0$ P26 line has varied. In 2006, the P26 line shows a red excess relative to the 2003 spectrum. In 2010, the excess shows a minimal Doppler shift (-1 ± 1 km s $^{-1}$) relative to 2003. In 2013, the P26 line shows a blueshifted excess.

(A color version of this figure is available in the online journal.)

vary relative to previous epochs (Figures 3(B) and 4(A)–(D)). We analyze the CO $v = 1-0$ emission using the procedure and rationale outlined in Paper II. We first normalize the spectrum so that the CO hotband lines have the same equivalent width as in the 2003 spectrum. Table 3 shows the scaled EW of the CO $v = 1-0$ emission in the resulting spectrum. We then subtract the 2003 spectrum to obtain the spectrum of the CO $v = 1-0$ excess emission component (Figure 4). The EW of the excess CO emission component and its velocity centroid and FWHM are shown in Table 3 where they are compared with the values from all earlier epochs.

As described in Paper II and summarized in Table 3, between 2003 and 2006, the red side of the P26 line brightened, the spatial offset of the red side of the line decreased, and the CO excess emission component had a velocity centroid of $+6 \pm 1$ km s $^{-1}$ (compare Figures 4(A) and (B)). Similarly, in 2010 the P26 line brightened further, and the excess emission was centered near zero velocity (-1 ± 1 km s $^{-1}$). In this part of the line profile, the spatial centroid of the line became offset further to the east (Figure 4(C)). In the 2013 epoch reported here, the blue side of the P26 line is again brighter than in 2003 and the excess is now blueshifted (-6 ± 1 km s $^{-1}$). The spatial centroid of the red side of the line is comparable to that in 2003 (Table 3), but the blue side of the line is now extended further to the east (Figure 4(D)).

4. DISCUSSION

4.1. Orbital Analysis

In Paper II, we suggested that the variations in the $v = 1-0$ line emission could be explained by the presence of a spatially concentrated source of CO emission that orbits the star within the disk wall. A schematic of this scenario is shown in Figure 4(E). We can obtain a rough constraint on the orbit of the CO excess component given the velocity centroids observed in 2006, 2010, and 2013. Assuming a system inclination of 42° (Ardila et al. 2007; Pineda et al. 2014) and a stellar mass of $2.4 M_\odot$, we fit a circular orbit to the measured velocities with the orbital radius R and the orbital phase of the excess in 2003 as free parameters. The result of a χ^2 fit (Figure 5) gives $R = 12.9^{+1.5}_{-1.3}$ AU and an orbital phase of $\phi = 6^{+15^\circ}_{-20^\circ}$, where $\phi = 0^\circ$ corresponds to the NW end of the semimajor axis. If we adopt a higher inclination (e.g., 50° ; compare for example Quanz et al. 2011 and Panić et al. 2014), our best fit shifts to $R = 14.0^{+1.6}_{-1.3}$ AU and an orbital phase of $\phi = 15^{+13^\circ}_{-15^\circ}$.

Hence, the velocity centroids at the three measured epochs are consistent with circular motion and locate the excess source

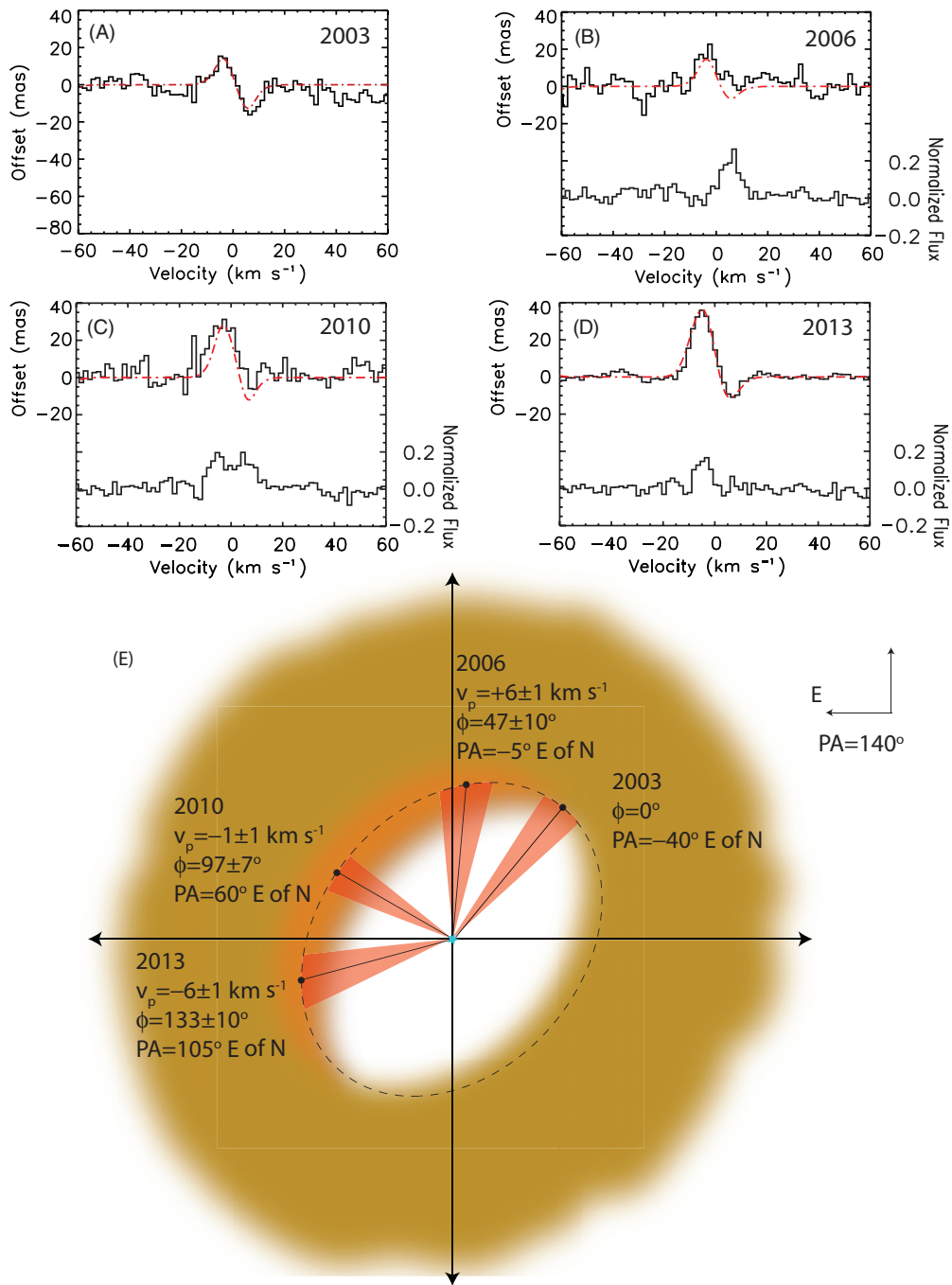


Figure 4. Spectroastrometric signal of the P26 line and schematic of the geometry of the system. In panels (A)–(D) the spectroastrometric signal of the P26 line is plotted. The excess flux of the P26 line is plotted below the spectroastrometric signal in panels (B)–(D). For each epoch the spectroastrometric signal is calculated from our excitation model with the excess emission added for the data acquired in 2006, 2010, and 2013 (red dot-dashed line). In panel (E), a schematic of the disk and extra emission source is presented. The orbit is represented by the black dashed line. The disk wall of the disk is shaded orange. The location of the source of the emission excess is labeled with a black dot, and the uncertainty in the phase of the orbit is represented by the red sectors. We assume the excess CO emission is hidden by the near side of the circumstellar disk in 2003. The phase of the orbit is calculated from the Doppler shift of the excess emission assuming the disk is inclined by 42° and the orbital radius is 12.5 AU (just inside the disk wall of the disk). In 2006, the excess emission pulled the center of light of the red side of the line closer to the center of the PSF. In 2010, the excess emission pulled both sides of the line eastward along the slit axis. In 2013, the excess emission on the blue side of the line pulled the spectroastrometric signal eastward.

(A color version of this figure is available in the online journal.)

in the vicinity of the disk wall. For an orbit with $R \simeq 12.5$ AU, the inferred orbital phase would locate the excess emission behind the disk wall (in projection) in 2003, hiding it from view, consistent with our use of 2003 as the reference epoch in this analysis (see also Paper II and Mulders et al. 2011). Figure 4(E) shows the velocities and implied position angles of the excess component.

To demonstrate that our spectroastrometric results are consistent with the above picture, we modeled the spectroastrometric signal that would be produced by the disk plus an extra source of CO emission in a circular orbit, following the method described in Paper II. Briefly, a CO emission component with the observed line profile of the excess emission is placed at the appropriate radius and phase in its orbit and added to our earlier

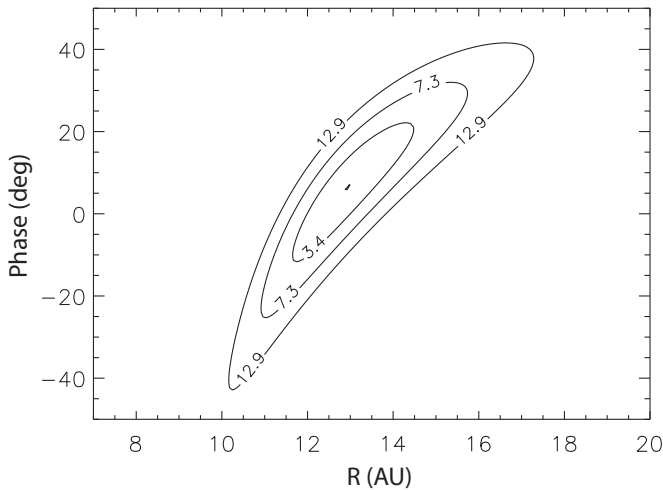


Figure 5. Constraint on the orbital radius R and orbital phase in 2003 ϕ placed by fitting the projected velocities and relative phases in 2006, 2010, and 2013, assuming the excess CO emission is in a circular Keplerian orbit and the inclination is 42° . The 1σ , 2σ , and 3σ confidence intervals are plotted. We find that $R = 12.9^{+1.5}_{-1.3}$ AU and $\phi = 6^{+15^\circ}_{-20^\circ}$.

model of CO emission from an eccentric disk wall and an axisymmetric circumstellar disk. Synthetic spectroastrometric signals are then calculated and compared with the observed values (Figures 4(A)–(D)).

In our model, the $5\ \mu\text{m}$ continuum arises from a compact source of emission within 1 AU of the star (Panić et al. 2014), thus to a very good approximation the center of the PSF is aligned with the star (within ~ 1 mas). The slit was aligned E–W in all four epochs presented in this paper, so the center of the PSF falls on the N–S line in our schematic (Figure 4(E)). For simplicity we adopt $R = 12.5$ AU and phase $= 0^\circ$ in 2003 for our calculation. As a result, the spectroastrometric signal of the P26 line at this epoch is consistent with emission arising from an axisymmetric disk (Figure 4(A)). As shown in Figures 4(B)–(D), the observed spectroastrometric signals in the subsequent epochs are well fit by our model of a compact source of emission in a Keplerian orbit near the disk wall, supporting our earlier interpretation (Paper II).

4.2. Comparison with Previous Results

In Papers I and II, we discussed two new lines of evidence for a massive substellar companion within the disk gap of HD 100546. In the first paper, we noted that the rovibrational OH emission lines from the disk are asymmetric and that the observed line profile can be explained by a disk with an eccentric inner rim. The OH line profiles can be reproduced if 75% of the OH emission arises from an annulus with an eccentricity of 0.18 ± 0.11 while the remainder arises from a circular outer disk. An inner rim with this level of eccentricity can arise from tidal interactions with a high-mass companion ($M \geq 3 M_{\text{Jup}}$; e.g., Kley & Dirksen 2006). The new observations reported here provide important support for the interpretation presented in Paper I. Dynamical studies that show how a giant planet can induce an eccentric inner rim also predict that the semi-major axis of the eccentric rim will precess very slowly ($\sim 10^\circ/1000$ orbits; Kley & Dirksen 2006). Hence, the asymmetric line profile from the rim is expected to be approximately constant in time. The OH line profiles we observe are consistent with this picture (Figure 3(A)).

In the second paper, we presented multi-epoch rovibrational CO emission and showed that the spectral shape and spectroastrometric signal of the $v = 1-0$ lines vary while those of the hotband lines do not. We showed that the variability of both the spectral shape and spectroastrometric signal of the $v = 1-0$ lines could be explained if a compact source of $v = 1-0$ emission orbits the star near the inner rim of the outer disk ($R \sim 13$ AU). We further suggested that the source of this orbiting CO emission is a circumplanetary disk. In the new CO observations reported here, both the velocity of the excess CO emission and the spectroastrometric signal reported here confirm our earlier interpretation of an emission source on a circular Keplerian orbit near the inner wall of the disk.

4.3. Origin of CO Emission: Circumplanetary Disk or Companion/Wall Interaction?

As discussed in Paper II, the luminosity of the excess CO emission is consistent with optically thick emission from a region with an emitting area of $\sim 0.1-0.2$ AU² for a temperature of 1400 K and a $3\ \text{km s}^{-1}$ intrinsic line width. This emitting area is a fraction of the size of a circumplanetary disk that is expected for a $5 M_{\text{J}}$ planet located 13 AU from a $2.4 M_\odot$ star. The assumed temperature of 1400 K seems plausible, because it is similar to that found for the inner circumplanetary disk in three-dimensional radiation hydrodynamical simulations (Klahr & Kley 2006; Gressel et al. 2013). As we also discussed in Paper II, the variability in the line profile and flux of the $v = 1-0$ excess emission component may be due to time variable circumplanetary disk accretion that results from either the predicted azimuthal variation in the accretion rate onto the circumplanetary disk (Kley & Dirksen 2006) and/or non-steady accretion through the circumplanetary disk (Martin & Lubow 2011a).

The interpretation that the excess $v = 1-0$ CO emission arises from a circumplanetary disk raises a couple of questions. One might wonder why the circumplanetary disk does not also produce observable CO hotband and OH emission. The lack of CO hotband emission is readily explained by the small emitting area ($0.1\ \text{AU}^2$) of the circumplanetary disk. Because the CO hotband emission is produced by UV fluorescence of disk gas, the resulting infrared lines are very optically thin, and the emission must extend over a much larger area to be observable. Our earlier detailed modeling of the hotband emission showed that the flux of the hotband lines could be explained by UV fluorescence of a thin layer of CO at the surface of the disk that extends from the disk wall to ~ 100 AU (Brittain et al. 2009).

The lack of a time variable OH excess component in the circumplanetary disk scenario is a more interesting question. The circumplanetary disk may not produce much OH emission if its atmosphere has a high dust-to-gas ratio. Because an atmosphere with a high dust abundance is well shielded from UV radiation, OH production via water photodissociation is less efficient, leading to a low OH abundance. The outer disk, if it is less well shielded by dust (e.g., as a result of grain growth and settling), could then dominate the OH emission from the system.

If the excess CO emission arises in a circumplanetary disk, observations of the kind presented here may lend insight into the nature of circumplanetary disks, which are thought to have complex dynamics. Hydrodynamical studies find that the accretion flow onto a planet is intrinsically three-dimensional, with the circumplanetary disk having a large-scale height ($H/R \sim 0.5$) and sub-Keplerian velocities (e.g., Klahr & Kley

2006; Ayliffe & Bate 2012). Inflow toward the planet is found to occur primarily downward from high latitudes, with material flowing outward in the midplane of the circumplanetary disk through most (e.g., Tanigawa et al. 2012; Gressel et al. 2013) or only the outer portion (Ayliffe & Bate 2012) of the disk. These ideas could potentially be explored with observations similar to those presented here. Because of the complex flow pattern, the expected line profile for CO emission from a circumplanetary disk will depend on where warm, dense CO is located, i.e., on the thermal-chemical properties of the region.

The limited constraints on the orbital radius of the CO excess emission component and the position of the disk wall (Section 4.1) allow for the possibility that the excess emission arises not from a discrete source (e.g., a circumplanetary disk), but instead from a localized region of the circumstellar disk, e.g., a CO bright spot on the disk wall. The bright spot could result from a local temperature or density enhancement. If it results from a temperature enhancement, both the CO and OH emission would be increased over that of the surrounding disk unless, e.g., the CO bright spot is also a region of high dust abundance, in which case the OH emission from the region may be suppressed (as discussed above).

Alternatively, because the CO $v = 1-0$ emission from HD 100546 appears to be subthermally excited (Brittain et al. 2009), the CO emission may be particularly sensitive to density enhancements. In contrast, the rovibrational OH emission is more likely to be in LTE given its much lower critical density⁷ and therefore insensitive to density. Detailed excitation modeling of the CO and OH emission from HD 100546 could be used to explore this and other potential explanations. If either a temperature or density enhancement turns out to be a viable explanation for the bright spot, it would be interesting to understand the physical origin of such a persistent enhancement, as the CO excess emission has now been observed over a 10 yr interval. Such enhancements might be induced by an orbiting giant planet (e.g., a local hot spot) or arise in structures associated with the planet (e.g., gap-crossing streams).

Higher angular resolution observations (e.g., with MagAO, GPI, SPHERE) can explore these scenarios by looking for evidence for an orbiting companion, a circumplanetary disk, or an emission bright spot on the disk wall. Observations made before 2017 have the best chance to detect the proposed orbiting structure before it is hidden by the disk wall. If the orbiting companion that we infer from our data is confirmed, along with that observed by Quanz et al. (2013) at larger orbital radii, we may be witnessing an example of multiple (perhaps even related, or sequential) planet formation in a circumstellar disk.

Based on observations collected at the European Organization for Astronomical Research in the Southern Hemisphere, Chile,

under program number 090.C-0571(A). S.D.B. acknowledges support for this work from the National Science Foundation under grant number AST-0954811. Basic research in infrared astronomy at the Naval Research Laboratory is supported by 6.1 base funding. J.N. gratefully acknowledges support from the Institute for Theory and Computation at the Harvard-Smithsonian Center for Astrophysics.

Facility: VLT:Antu (CRIRES)

REFERENCES

- Acke, B., & van den Ancker, M. E. 2006, *A&A*, 449, 267
 Ardila, D. R., Golimowski, D. A., Krist, J. E., et al. 2007, *ApJ*, 665, 512
 Atahan, S., & Alexander, M. H. 2006, *JPCA*, 110, 5436
 Ayliffe, B. A., & Bate, M. R. 2009, *MNRAS*, 397, 657
 Ayliffe, B. A., & Bate, M. R. 2012, *MNRAS*, 427, 2597
 Benisty, M., Tatulli, E., Ménard, F., & Swain, M. R. 2010, *A&A*, 511, A75
 Bouwman, J., de Koter, A., Dominik, C., & Waters, L. B. F. M. 2003, *A&A*, 401, 577
 Brittain, S. D., Najita, J. R., & Carr, J. S. 2009, *ApJ*, 702, 85
 Brittain, S. D., Najita, J. R., Carr, J. S., et al. 2013, *ApJ*, 767, 159
 Brittain, S. D., Simon, T., Najita, J. R., & Rettig, T. W. 2007, *ApJ*, 659, 685
 Carmona, A., van der Plas, G., van den Ancker, M. E., et al. 2011, *A&A*, 533, A39
 Close, L. M., Follette, K. B., Males, J. R., et al. 2014, *ApJL*, 781, L30
 Grady, C. A., Woodgate, B., Heap, S. R., et al. 2005, *ApJ*, 620, 470
 Gressel, O., Nelson, R. P., Turner, N. J., & Ziegler, U. 2013, *ApJ*, 779, 59
 Guimarães, M. M., Alencar, S. H. P., Corradi, W. J. B., & Vieira, S. L. A. 2006, *A&A*, 457, 581
 Habart, E., Natta, A., Testi, L., & Carillet, M. 2006, *A&A*, 449, 1067
 Hein Bertelsen, R. P., Kamp, I., Goto, M., et al. 2014, *A&A*, 561, A102
 Helled, R., Bodenheimer, P., Podolak, M., et al. 2013, in *Protostars and Planets VI*, in press (arXiv:1311.1142)
 Henning, T., Burkert, A., Launhardt, R., Leinert, C., & Stecklum, B. 1998, *A&A*, 336, 565
 Huélamo, N., Lacour, S., Tuthill, P., et al. 2011, *A&A*, 528, L7
 Klahr, H., & Kley, W. 2006, *A&A*, 445, 747
 Kley, W., & Dirksen, G. 2006, *A&A*, 447, 369
 Kraus, A. L., & Ireland, M. J. 2012, *ApJ*, 745, 5
 Kunde, V. R., & Maguire, W. C. 1974, *JQSRT*, 14, 803
 Liskowsky, J. P., Brittain, S. D., Najita, J. R., et al. 2012, *ApJ*, 760, 153
 Liu, W. M., Hinz, P. M., Meyer, M. R., et al. 2003, *ApJL*, 598, L111
 Manoj, P., Bhatt, H. C., Maheswar, G., & Muneer, S. 2006, *ApJ*, 653, 657
 Martin, R. G., & Lubow, S. H. 2011, *ApJL*, 740, L6
 Mulders, G. D., Paardekooper, S.-J., Panić, O., et al. 2013, *A&A*, 557, A68
 Mulders, G. D., Waters, L. B. F. M., Dominik, C., et al. 2011, *A&A*, 531, A93
 Panić, O., Ratzka, T., Mulders, G. D., et al. 2014, *A&A*, 562, A101
 Pineda, J. E., Quanz, S. P., Meru, F., et al. 2014, *ApJL*, 788, L34
 Pogodin, M. A., Hubrig, S., Yudin, R. V., et al. 2012, *AN*, 333, 594
 Quanz, S. P., Amara, A., Meyer, M. R., et al. 2013, *ApJL*, 766, L1
 Quanz, S. P., Schmid, H. M., Geissler, K., et al. 2011, *ApJ*, 738, 23
 Rothman, L. S., Barbe, A., Benner, D. C., et al. 2003, *JQSRT*, 82, 5
 Tanigawa, T., Ohtsuki, K., & Machida, M. N. 2012, *ApJ*, 747, 47
 Thi, W. F., Kamp, I., Woitke, P., et al. 2013, *A&A*, 551, A49
 van den Ancker, M. E., The, P. S., Tjin A Dje, H. R. E., et al. 1997, *A&A*, 324, L33
 van der Plas, G., van den Ancker, M. E., Acke, B., et al. 2009, *A&A*, 500, 1137
 van Leeuwen, F. 2007, *A&A*, 474, 653

⁷ Atahan & Alexander (2006) find that the collisional deexcitation rate out of OH $v = 1$ at 300 K is $2 \times 10^{-10} \text{ cm}^3 \text{ s}^{-1} \text{ mol}^{-1}$, or three orders of magnitude larger than the rate for CO at 300 K (Thi et al. 2013). Given the similarity of the transition probabilities for OH and CO, this implies that the critical density of OH is three orders of magnitude lower than that of CO at this temperature. Modeling of the excitation of OH requires determination of the collisional deexcitation rate at higher temperatures.